ADVANCED OPTICAL MATERIALS
www.advopticalmat.de

Nonlinear Dispersion Relation and Out-of-Plane Second Harmonic Generation in MoSSe and WSSe Janus Monolayers

Marko M. Petrić, Viviana Villafañe, Paul Herrmann, Amine Ben Mhenni, Ying Qin, Yasir Sayyad, Yuxia Shen, Sefaattin Tongay,* Kai Müller, Giancarlo Soavi,* Jonathan J. Finley, and Matteo Barbone**

Janus transition metal dichalcogenides are an emerging class of atomically thin materials with engineered broken mirror symmetry that gives rise to long-lived dipolar excitons, Rashba splitting, and topologically protected solitons. They hold great promise as a versatile nonlinear optical platform due to their broadband harmonic generation tunability, ease of integration on photonic structures, and nonlinearities beyond the basal crystal plane. Here, second and third harmonic generation in MoSSe and WSSe Janus monolayers is studied. Polarization-resolved spectroscopy is used to map the full second-order susceptibility tensor of MoSSe, including its out-of-plane components. In addition, the effective third-order susceptibility and the second-order nonlinear dispersion close to exciton resonances for both MoSSe and WSSe are measured at room and cryogenic temperatures. This work sets a bedrock for understanding the nonlinear optical properties of Janus transition metal dichalcogenides and probing their use in the next-generation on-chip multifaceted photonic devices.

1. Introduction

Nonlinear optics with atomically thin and layered materials has proven to be a powerful spectroscopic approach to study the physics of excitons confined at the ultimate thickness limit, as well as a fruitful playground to test novel ultrafast and ultrathin optical devices.[1] Parametric harmonic generation has been used to probe interlayer excitons in homo-[2] and hetero-bilayers,[3] and to detect quantum interference pathways and strong coupling in monolayer transition metal dichalcogenides (TMDs).[4] Furthermore, nonlinear optical properties of layered materials are adding a rapidly growing number of applications in optics, which already include electrical[5] and all-optical[6] ultrafast and broadband frequency converters, miniaturized logic gates,[7,8] photonic integrated gas sensors,[9] nonlinear holograms,[10] and ultrathin quantum sources based on spontaneous parametric down conversion (SPDC).[11]

Lately, a new class has expanded the family of atomically thin materials: Janus transition metal dichalcogenide (Janus TMD) monolayers are van der Waals materials with different chalcogen atoms within the crystal unit cell, which breaks mirror symmetry, and creates an out-of-plane electrical polarity due to charge imbalance.[12–14] The structural mirror-symmetry breaking in Janus TMD monolayers gives rise to

M. M. Petrić, K. Müller, M. Barbone
Walter Schottky Institut and Department of Electrical and Computer Engineering
Technische Universität München, Am Coulombwall 4
85748 Garching, Germany
E-mail: marko.petric@wsi.tum.de; Matteo.Barbone@wsi.tum.de
M. M. Petrić, V. Villafañe, A. Ben Mhenni, K. Müller, J. J. Finley, M. Barbone
Munich Center for Quantum Science and Technology (MCQST)
Schellingstrasse 4, 80799 Munich, Germany

The ORCID identification number(s) for the author(s) of this article can be found under https://doi.org/10.1002/adom.202300958

DOI: 10.1002/adom.202300958

V. Villafañe, A. Ben Mhenni, J. J. Finley
Walter Schottky Institut and Physik-Department
Technische Universität München, Am Coulombwall 4
85748 Garching, Germany
P. Herrmann, G. Soavi
Institute of Solid State Physics
Friedrich Schiller University Jena
Max-Wien-Platz 1, 07743 Jena, Germany
E-mail: giancarlo.soavi@uni-jena.de
Y. Qin, Y. Sayyad, Y. Shen, S. Tongay
Materials Science and Engineering
School for Engineering of Matter
Transport and Energy, Arizona State University
Tempe, Arizona 85287, USA
E-mail: sefaattin.tongay@asu.edu
G. Soavi
Abbe Center of Photonics
Friedrich Schiller University Jena
Albert-Einstein-Straße 6, 07745 Jena, Germany

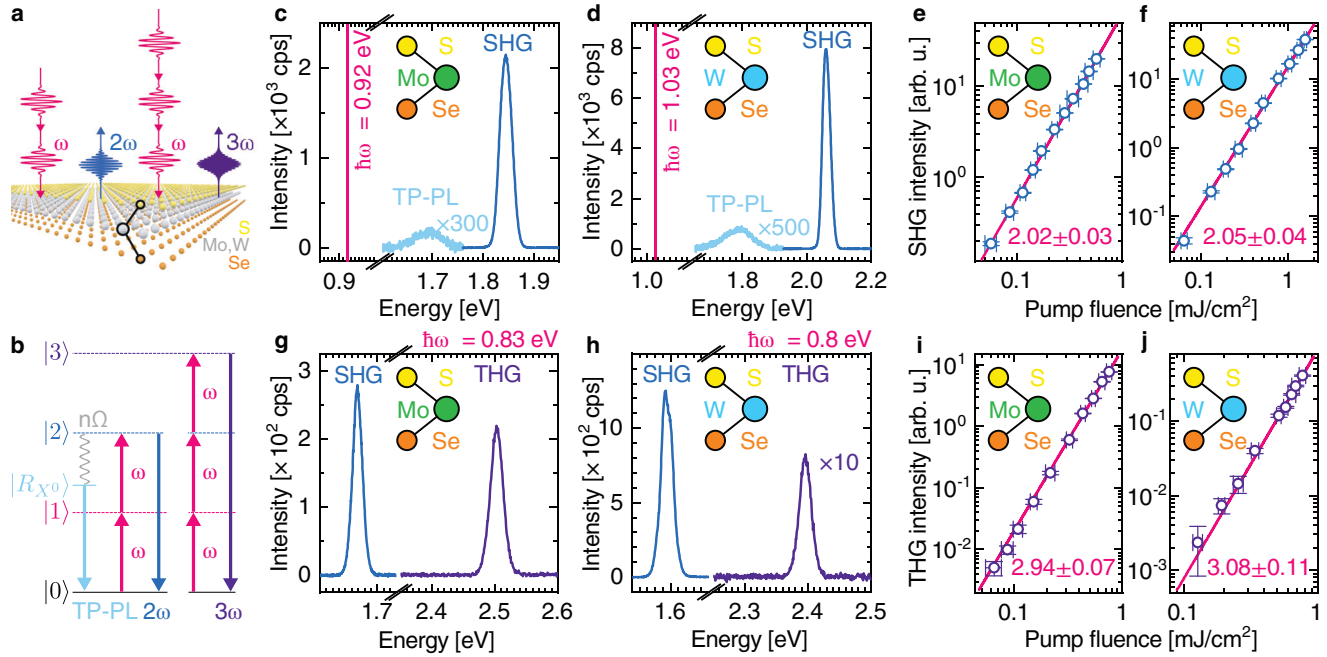

Figure 1. SHG and THG in MoSSe and WSSe Janus monolayers. a) Schematic representation of a Janus TMD monolayer and the reflection measurement geometry. b) Schematic representation of SHG (blue), THG (purple), and TP-PL (light blue) transitions under two- and three-photon excitation with angular frequency ω (magenta) between the excited levels $|1\rangle$, $|2\rangle$, $|3\rangle$, the real exciton level $|R_{X^0}\rangle$, linked via single- or multi-phonon channel $n\Omega$ to $|2\rangle$ (gray), and the ground state $|0\rangle$. c,d) Measured spectra showing SHG (blue) and scaled TP-PL (light blue) peaks stemming from c) MoSSe and d) WSSe Janus monolayer upon two-photon excitation (magenta). e,f) Respective SHG peak intensities as a function of pump fluence show quadratic increase as extracted from the power law fit (magenta). g,h) THG (purple) and SHG (blue) spectra of g) MoSSe Janus monolayer with excitation energy $\hbar\omega = 0.83$ eV and h) WSSe Janus monolayer with excitation energy $\hbar\omega = 0.8$ eV. i,j) Respective THG peak intensities as a function of pump fluence show cubic slopes as extracted from the power law fit (magenta).

physical effects and functionalities beyond those offered by conventional TMDs, such as Rashba spin-splitting,[15–20] and topologically-protected and localized solitonic spin textures.[21–23] Moreover, due to the reduced overlap between electron and hole wavefunctions, Janus TMD monolayers host longer-lived dipolar excitons than mirror-symmetric TMDs,[24–27] making them a potential platform for exciton Bose-Einstein condensation and other strongly correlated many-body states.[28] Since their theoretical prediction in 2013[15] and first synthesis in 2017[29,30] a multitude of morphotaxy-based techniques[31] have emerged breaching bottlenecks toward the synthesis of high-quality MoSSe and WSSe Janus monolayers.[32–38] Further studies have already provided insight into their vibrational properties,[39,40] interlayer coupling strength,[27,41,42] exciton complexes,[43] second harmonic generation,[44] and dipole emission profile.[45]

Atomically thin crystals provide two distinct advantages compared to conventional bulk materials used in nonlinear optics. First, a high degree of compatibility with on-chip photonic architectures.[46–49] Second, their atomically thin nature combined with a strong nonlinear response[1,50] allows for efficient frequency conversion without phase matching constraints,[51,52] and thus, provides a viable route towards ultra-broadband classical and quantum sources of light. Janus TMD monolayers further expand such advantages by respectively adding out-of-plane components in the nonlinear optical response,[53–55] which introduce an additional functionality to be harnessed in vertical photonics structures,[56,57] and widening the spectral region of resonantly enhanced nonlinear optics to different areas of the visible and near-infrared light.[58] To capitalize on such advantages, understanding the wavelength-dependent second harmonic generation (SHG) efficiency (i.e., the nonlinear dispersion) and mapping the corresponding susceptibility tensor in Janus TMD monolayers is essential.

In this work, we address both these open issues and provide a detailed study of the out-of-plane second-order nonlinear susceptibility in MoSSe Janus monolayer, using a simplified approach that fully maps the susceptibility tensor using a high numerical aperture (NA) objective. Furthermore, we measure third harmonic generation (THG) and the wavelength-dependent SHG efficiency of MoSSe and WSSe Janus monolayers, revealing the *A* and *B* exciton resonances at room and cryogenic temperatures.

2. Results and Discussion

Janus TMD monolayers were fabricated via a room temperature selective epitaxy atomic replacement method.[33] In this process, the top-layer selenium atoms in previously grown $MoSe_2$ (on Si/SiO_2) and WSe_2 (on Al_2O_3) parent monolayers are replaced by sulfur atoms, resulting in MoSSe and WSSe Janus monolayers, respectively, schematically represented in **Figure 1**a. We studied their nonlinear optical response at room and cryogenic temperatures by focusing linearly polarized pulsed light of angular frequency ω onto the crystal, and detecting the outgoing light in reflection geometry, as illustrated in Figure 1a. In particular, we

used 100-fs pulses with a repetition rate of 80 MHz generated by a tunable optical parametric oscillator (OPO) and pumped by a mode-locked Ti:sapphire laser (see Experimental section).

MoSSe and WSSe Janus monolayers are non-centrosymmetric crystals,[15] and thus, possess nonvanishing even-order terms in the polarization vector expansion. As a result, they exhibit a distinct second harmonic (SH) overtone induced by a light field of frequency ω:[59,60]

$$P_i^{(2)}(2\omega) = \epsilon_0 \sum_{j,k} \chi_{ijk}^{(2)}(2\omega;\omega,\omega) E_j(\omega) E_k(\omega) \tag{1}$$

here, Cartesian components of the second-order polarization vector $\mathbf{P}^{(2)}(2\omega)$ capture the material's response to the interaction with an external optical field $\mathbf{E}(\omega)$. The two vectors are linked via a third-rank tensor $\chi^{(2)}(2\omega;\omega,\omega)$, which can be directly deduced from the crystal symmetry. SHG is a parametric process where the annihilation of two photons of frequency ω is followed by the creation of a single photon of frequency 2ω. The photons link (virtual or real) excited states $|1\rangle$ and $|2\rangle$ to the electronic ground state $|0\rangle$,[60,61] as illustrated in Figure 1b. In contrast, THG exists irrespective of the inversion symmetry and involves three annihilated photons of energy $\hbar\omega$ and a created photon of energy $3\hbar\omega$ from a state $|3\rangle$ denoted in purple in Figure 1b. Analogously to Equation (1), third-order polarization properties of a crystal are dictated by a fourth-rank tensor $\chi^{(3)}(3\omega;\omega,\omega,\omega)$.[60] In the case of TMDs, upon a two-photon excitation, the system may in addition relax via $n = 1,2,3,\cdots$ phonons Ω[62] through a two-photon photoluminescence (TP-PL) involving a real exciton state $|R_{X^0}\rangle$,[63] denoted in light blue.

Figure 1c(d) shows the detected light from MoSSe (WSSe) Janus monolayer at room temperature using $\hbar\omega = 0.92$ eV ($\hbar\omega = 1.03$ eV) excitation energy. We choose these specific energies to separate the SHG and TP-PL signals. For both materials, we detect a pronounced SHG signal (blue) and less efficient TP-PL signal (light blue) at a photon energy corresponding to the 1*s* neutral exciton X^0 at ≈1.69 eV (≈1.79 eV).[39] Figure 1e,f show the power dependence of the SH signal for MoSSe and WSSe Janus monolayers, respectively, confirming the SH nature of the signal at $2\hbar\omega$ via the canonical quadratic increase in the SH peak power as a function of pump fluence.[60,64,65] In addition, we measure circular polarization selection rules consistent with SHG (see Section S1, Supporting Information).

We also observe THG signals: Figure 1g,h show room temperature SHG and THG spectra of MoSSe and WSSe Janus monolayers for excitation energies $\hbar\omega = 0.83$ eV and $\hbar\omega = 0.8$ eV, respectively. To confirm the third harmonic (TH) nature of the signal, we again perform power-dependent measurements, which exhibit power law dependencies with near cubic behavior, as expected.[66–69] The results are presented in Figure 1i for MoSSe, and Figure 1j for WSSe Janus monolayer, respectively. The intensity of the nonlinear response is normally expected to drop with increasing nonlinear order. However, for low pumping energies, TMDs exhibit a higher THG compared to the SHG signal due to nearly rotationally invariant bands only corrected by trigonal warping of the valence and conduction bands.[68,70] MoSSe Janus monolayers conform to this behavior, exhibiting comparable SHG and THG signals, as shown in Figure 1g. Here, THG does not dominate over SHG because the latter is close to resonance with the *A* exciton. Furthermore, we derive the value of the effective third-order susceptibility (see Section S2, Supporting Information) and obtain $\chi_{\text{eff}}^{(3)}(\hbar\omega = 0.8\,\text{eV}) = 1.55 \times 10^5\ \text{pm}^2\text{V}^{-2}$, which is close to reported values for other TMDs.[50,66–69] In terms of harmonic efficiency, defined as the ratio of THG peak power to incident power, we obtain $\approx 3 \times 10^{-11}$ for an incident power of 20 mW. Interestingly, in a WSSe Janus monolayer the SHG intensity dominates over the THG, in contrast to all measurements on TMDs reported to date. For WSSe Janus monolayer, the measured effective third-order susceptibility is $\chi_{\text{eff}}^{(3)}(\hbar\omega = 0.83\ \text{eV}) = 1.52 \times 10^5\ \text{pm}^2\text{V}^{-2}$, and the harmonic efficiency is $\approx 10^{-11}$ for an incident power of 20 mW.

Next, we shift our attention to the study of the out-of-plane second-order nonlinear response of MoSSe Janus monolayer. In contrast to conventional TMDs, which belong to the D_{3h} point group, the lack of mirror symmetry puts Janus TMD monolayers in the C_{3v} point group, which displays five independent nonzero components $\chi_{xzx}^{(2)} = \chi_{yzy}^{(2)}$, $\chi_{xxz}^{(2)} = \chi_{yyz}^{(2)}$, $\chi_{zxx}^{(2)} = \chi_{zyy}^{(2)}$, $\chi_{zzz}^{(2)}$, $\chi_{yyy}^{(2)} = -\chi_{yxx}^{(2)} = -\chi_{xxy}^{(2)} = -\chi_{xyx}^{(2)}$. Furthermore, the Kleinman's symmetry condition in SHG always allows to permute the last two indices;[60] thus, $\chi_{xzx}^{(2)} = \chi_{xxz}^{(2)}$. Finally, we explicitly write the susceptibility tensor $\chi_{C_{3v}}^{(2)}(2\omega;\omega,\omega)$ in contracted notation[60] by rewriting Equation (1) in a matrix form:

$$\begin{pmatrix} P_x^{(2)}(2\omega) \\ P_y^{(2)}(2\omega) \\ P_z^{(2)}(2\omega) \end{pmatrix} = \epsilon_0 \begin{pmatrix} 0 & 0 & 0 & 0 & \chi_{xxz}^{(2)} & -\chi_{yyy}^{(2)} \\ -\chi_{yyy}^{(2)} & \chi_{yyy}^{(2)} & 0 & \chi_{xxz}^{(2)} & 0 & 0 \\ \chi_{zxx}^{(2)} & \chi_{zxx}^{(2)} & \chi_{zzz}^{(2)} & 0 & 0 & 0 \end{pmatrix} \begin{pmatrix} E_x(\omega)E_x(\omega) \\ E_y(\omega)E_y(\omega) \\ E_z(\omega)E_z(\omega) \\ 2E_y(\omega)E_z(\omega) \\ 2E_x(\omega)E_z(\omega) \\ 2E_x(\omega)E_y(\omega) \end{pmatrix} \tag{2}$$

Equation (2) implies two distinct features: i) the presence of a nonvanishing out-of-plane $P_z^{(2)}(2\omega)$ polarization, as illustrated in the blue inset in **Figure 2**a, and ii) the introduction of additional terms to the polarization vector components by an out-of-plane driving field $E_z(\omega)$, which can be activated by exciting the crystal at an angle, as illustrated in Figure 2a with a magenta line.

The experimentally accessible SHG intensity components can be conveniently derived from the polarization $P_{x,y,z}^{(2)}(2\omega)$ by introducing a polar coordinate system, as shown in Figure 2b.

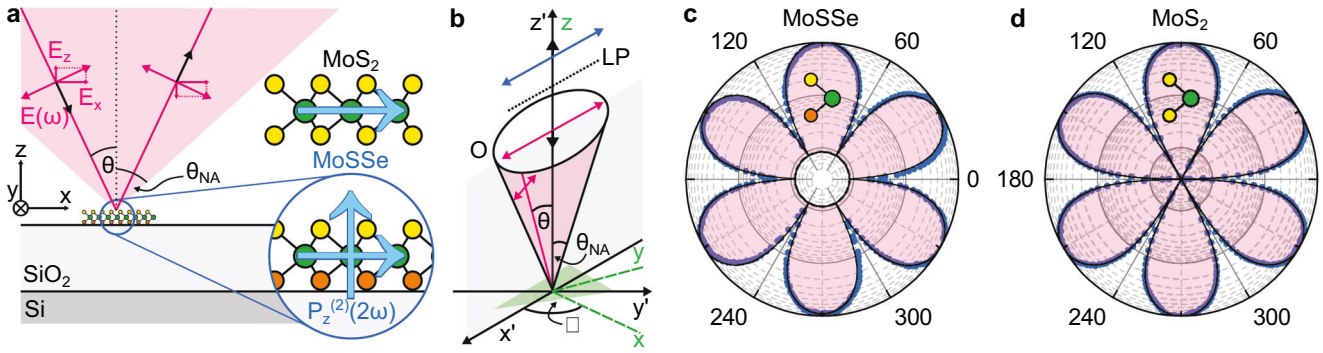

Figure 2. Out-of-plane polarization dipole in MoSSe Janus monolayer. a) Schematic representation of the out-of-plane SH excitation and detection. Magenta denotes light incident along an angle θ from the optical axis, limited to θ_{NA} by the objective numerical aperture. MoSSe Janus monolayer possesses the $P_z^{(2)}(2\omega)$ component contrasting with the MoS_2 monolayer that only has an in-plane polarization component. b) Schematic representation of the measurement configuration in a polar coordinate system. Excitation (magenta) and detection (blue) light have the same polarization entering and exiting the objective (O) determined with a linear polarizer (LP). Angle ϕ follows the crystal orientation. The crystal frame is highlighted in green. c,d) Logarithmic polar plots of the normalized polarization-resolved SHG intensity of c) Janus MoSSe and d) MoS_2 monolayer. Measured intensity is represented with blue data points, the fitting curve in black, and the shaded region in pink is bound by the minimum of the fitting function.

The resulting SHG intensity components in the crystal frame of reference are:

$$I_x \propto \left|\chi^{(2)}_{xxz} \sin 2\theta + \chi^{(2)}_{yyy} \cos^2\theta \sin 3\phi\right|^2 \quad (3)$$

$$I_y \propto \left|\chi^{(2)}_{yyy} \cos^2\theta \cos 3\phi\right|^2 \quad (4)$$

$$I_z \propto \left|\chi^{(2)}_{zxx} \cos^2\theta + \chi^{(2)}_{zzz} \sin^2\theta\right|^2 \quad (5)$$

where θ is the incidence angle of excitation, and ϕ is the angle between the crystal zigzag direction (x-axis) and the x' excitation and detection axis in the laser frame of reference [55]. In contrast, the SHG intensity components stemming from D_{3h} TMDs are [55,65,71]:

$$I_x \propto \left|\chi^{(2)}_{yyy} \cos^2\theta \sin 3\phi\right|^2 \quad (6)$$

$$I_y \propto \left|\chi^{(2)}_{yyy} \cos^2\theta \cos 3\phi\right|^2 \quad (7)$$

To extract the susceptibility tensor components of Janus TMD monolayers, we measure the SHG intensity as a function of the rotation angle ϕ in a co-polarized configuration (see Experimental Section). This is equivalent to rotating the crystal in the laser frame of reference. We use the aforementioned equations to model the experimentally collected SHG light intensity $I_p = I_x \cos^2\theta + I_z \sin^2\theta$, which sums both components present in the plane of incidence. We used a high-NA objective (NA = 0.75), which enables large angles θ for strong out-of-plane driving and high detection efficiency of the out-of-plane polarization component. This approach simplifies the methods previously employed to retrieve non-planar components[29,72] and can easily be generalized for any material of a similar symmetry. Figure 2c plots normalized I_p as a function of ϕ on a logarithmic scale measured from a MoSSe Janus monolayer excited at $\hbar\omega = 0.885$ eV, away from the A exciton resonance to avoid the TP-PL signal that could be unpolarized, and thus, could leave residual signals in the polarization-dependent SHG experiment that are difficult to deconvolve. Following Equations (3) and (5), we expect that out-of-plane susceptibility components $\chi^{(2)}_{xxz}$, $\chi^{(2)}_{zxx}$, and $\chi^{(2)}_{zzz}$ contribute to the nonvanishing I_p for all angles ϕ. Indeed, the flower pattern 'opens up', never reaching zero, as shown in Figure 2c by the non-shaded region where the upper border represents the minimum value of the fitting function in black given by Equation (S33) (see Section S3, Supporting Information). Here, we take into account the angle-dependent substrate reflection and integrate the resulting intensity over the angle θ for the entire NA of the objective as explained in Section S3 (Supporting Information). In comparison, Figure 2d shows normalized polarization-resolved SHG intensity of a reference MoS_2 monolayer for the same excitation energy and the same-scaled logarithmic polar plot. I_p follows the characteristic six-fold pattern given by Equation (6), which goes to zero when excitation polarization is aligned with the zigzag crystal edge,[64,65,71] strongly contrasting with the MoSSe Janus monolayer in Figure 2c (see Section S4, Supporting Information).

We now turn to disentangling the complex interplay of all susceptibility components contributing to the SHG intensity I_p. In order to give a quantitative estimate of the out-of-plane components compared to the in-plane components, we simplify the $\chi^{(2)}$ tensor by imposing the Kleinman's symmetry assuming dispersionless response at both ω and 2ω to obtain $\chi^{(2)}_{xxz} = \chi^{(2)}_{zxx}$.[29,60] This is possible since under these specific experimental conditions the SHG process is performed far off exciton resonances. We further reduce the number of parameters by introducing a $\chi^{(2)}_{zzz}/\chi^{(2)}_{xxz}$ ratio deduced from theoretical calculations.[55] As a final result, we obtain $\chi^{(2)}_{yyy}/\chi^{(2)}_{xxz} = 8.4$ at $\hbar\omega = 0.885$ eV pumping (see Section S3, Supporting Information), which is comparable to theoretically calculated values.[55] Thus, with our simple approach, we are able to fully map the second-order susceptibility tensor in MoSSe Janus monolayer. MoSSe and WSSe Janus monolayers both belong to the C_{3v} point group. Therefore, we expect the same qualitative trend, i.e., non-vanishing component of the out-of-plane SHG, also for WSSe Janus monolayer.

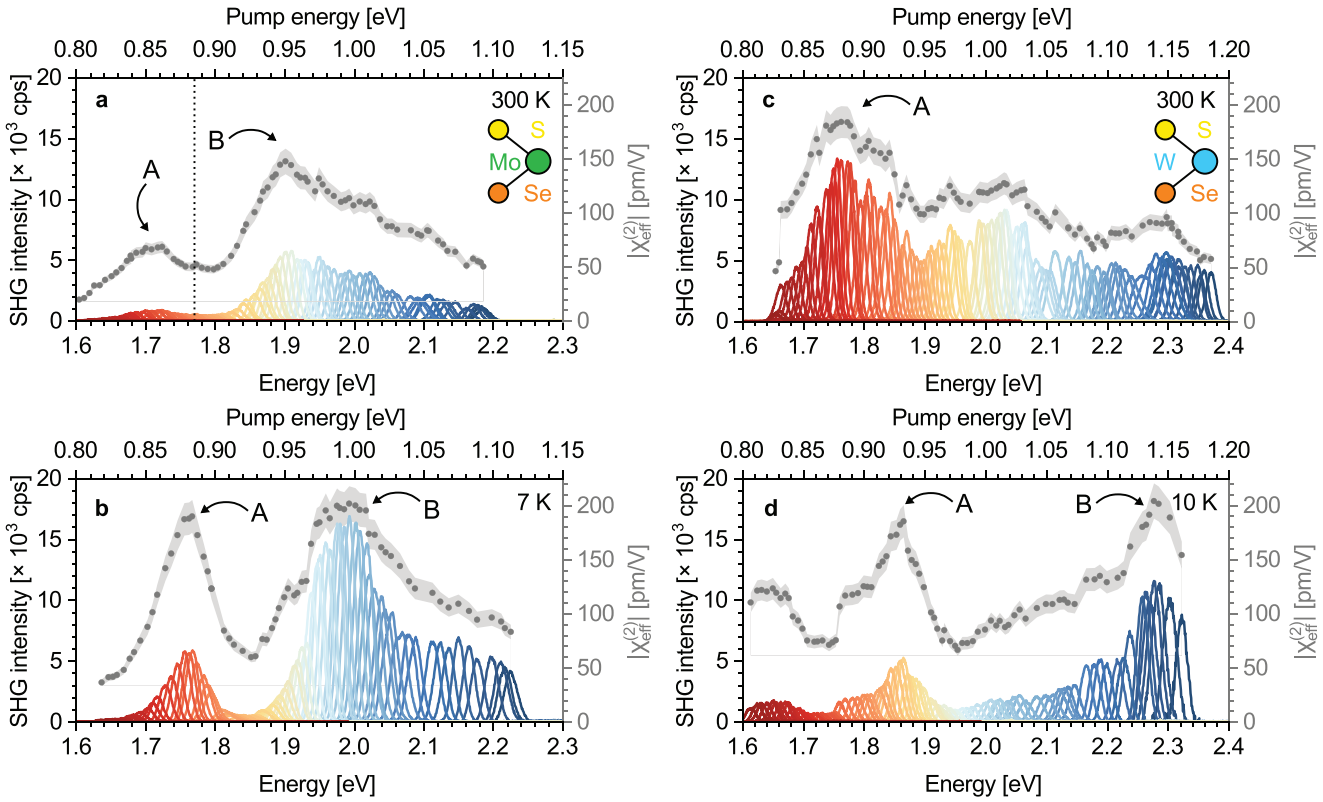

Figure 3. SHG enhancement at exciton resonances and $\chi^{(2)}_{yyy}$ dispersion. a,b) SHG spectra from MoSSe Janus monolayer as a function of two-photon energy (bottom *x*-axis) and pump energy (top *x*-axis) at a) $T = 300$ K and b) $T = 7$ K with $\chi^{(2)}_{yyy}$ dispersion represented in gray points within a light gray error band. c,d) SHG spectra from WSSe Janus monolayer as a function of two-photon energy and pump energy at c) $T = 300$ K and d) $T = 10$ K with $\chi^{(2)}_{yyy}$ dispersion represented in gray points within a light gray error band. Assignments of *A* and *B* excitons are denoted by arrows.

Finally, we discuss the second-order nonlinear dispersion at room and cryogenic temperatures in MoSSe and WSSe Janus monolayers, focusing on the in-plane component $\chi^{(2)}_{yyy}$ of the nonlinear susceptibility. For this purpose, we use a low-NA objective (NA = 0.3) to quench the non-planar components with negligible out-of-plane driving (see Figure S3e, Supporting Information). **Figure 3**a,b show MoSSe Janus monolayer wavelength-dependent SHG spectra at room and cryogenic temperatures, respectively, obtained by sweeping the pumping energy, while maintaining constant pumping power. From the SHG intensities, we can derive the absolute values of the corresponding effective bulk-like second-order susceptibility dispersion $\chi^{(2)}_{yyy}$,[50,67] presented in gray points and gray error band to account for excitation power fluctuations (see Section S2, Supporting Information). For $\hbar\omega = 0.885$ eV excitation, we measure $\chi^{(2)}_{yyy} = 51$ pmV^{-1}. Then, we straightforwardly obtain the other components $\chi^{(2)}_{xxz} = \chi^{(2)}_{zxx} = 6$ pmV^{-1}, and $\chi^{(2)}_{zzz} = 1.5$ pmV^{-1}, where $\chi^{(2)}_{yyy}$ is highlighted in Figure 3a by the dotted line. Furthermore, when resonant with a real state, SHG is strongly enhanced[63] and it can thus be used as a background- and absorption-free spectroscopic tool to map the exciton states of Janus TMD monolayers. For the MoSSe Janus monolayer, we observe pronounced resonances corresponding to the *A* and *B* excitons, and note that the *A* to *B* exciton $\chi^{(2)}_{yyy}$ ratio evolves from the *B* exciton dominating at room temperature to being the same as the *A* exciton at $T = 7$ K. This is in clear contrast to the WSSe Janus monolayer in Figure 3c,d at room and cryogenic temperatures, respectively. While *A* and *B* show similar values at $T = 10$ K, *A* dominates over *B* at room temperature. In addition, the WSSe Janus monolayer dispersion shows additional resonances below 1.8 eV the origin of which remains unclear at present and requires further study. We tentatively ascribe them to charged excitons or defect bands. While we studied SHG dispersion in the *A* and *B* exciton range, another theoretically predicted resonance[53] has been observed in MoSSe monolayer close to 2.75 eV.[44]

In our experiments, the SH susceptibility of MoSSe and WSSe Janus monolayers at room temperature at exciton resonances is $\chi^{(2)}_{yyy} \approx 150$ pmV^{-1}, and 200 pmV^{-1}, respectively, which is among the largest reported values of second-order susceptibilities for any TMD monolayer.[73] In addition, we draw a qualitative and quantitative comparison between the measured dispersion in the MoSSe Janus monolayer and the corresponding calculations available in the literature[53–55] (see Section S5, Supporting Information). Reference [55] shows nearly dispersionless results in the exciton-dominated region, while references [53] and [54] display two distinct resonances that align closely with the measured *A* and *B* excitons, providing a good qualitative agreement to the experimental data. Under quantitative comparison,

experimental values consistently exhibit lower values compared to theoretical predictions. This is not surprising, as significant discrepancies are already reported between the calculated results (due to different calculation methods and corrections, excitonic effects, screening, temperature effects, etc.), while further reduction of the signal may be due to suboptimal sample quality.

3. Conclusion

In summary, we studied optical nonlinearities in MoSSe and WSSe Janus monolayers. We found an unusually low TH intensity in WSSe. In addition, we introduced a simple method to study their out-of-plane nonlinear susceptibility and measured values of $\chi^{(2)}_{xxz} = \chi^{(2)}_{zxx} = 6\ \mathrm{pmV^{-1}}$ and $\chi^{(2)}_{zzz} = 1.5\ \mathrm{pmV^{-1}}$ in MoSSe Janus monolayer. Finally, we provide the susceptibility dispersion on and off resonance across the exciton spectrum of both materials at room and cryogenic temperatures. Close to exciton resonances, we measured up to $\chi^{(2)}_{yyy} \approx 200\ \mathrm{pmV^{-1}}$ for the in-plane SH nonlinear susceptibility, a value that is among the largest measured for atomically thin materials. Our work establishes a solid foundation to understand the nonlinear optical response of Janus TMD monolayers and their use in applications such as broadband frequency conversion and nonlinear photonic integrated circuits. Future steps should address two key challenges: i) the comparatively low total efficiency; ii) integration on-chip/fiber, which is one way to enhance the total nonlinear response and, thus, efficiency. However, in the latter, phase-matching conditions need to be considered. This has already been successfully demonstrated for conventional TMDs,[49] while the direct growth of Janus TMD on-chip and photonic platforms is yet to be reported.

4. Experimental Section

Samples: Janus TMD monolayers were synthesized via a room temperature selective epitaxy atomic replacement method thoroughly explained in ref. [33]. MoSSe and WSSe Janus monolayers lay on Si/SiO_2 and Al_2O_3 substrates, respectively. The reference MoS_2 monolayer was encapsulated in thin hBN (HQ Graphene) and prepared on a Si/SiO_2 substrate with the same thickness as for MoSSe Janus monolayer. SHG maps from prototypical MoSSe and WSSe Janus monolayers were presented in Section S6 (Supporting Information).

Optical Measurements: 100-fs pulsed laser was used for SHG and THG measurements with a repetition rate of 80 MHz generated from an OPO (Levante IR fs, A.P.E.; and Inspire Femtosecond OPO, Radiantis) and pumped by a mode-locked Ti:sapphire laser, which was followed by a linear polarizer to ensure fixed excitation polarization.

For the polarization-resolved SHG measurements, a high-NA objective (NA = 0.75, Objective LD Plan-Neofluar 63x/0.75 Corr M27, Zeiss) was used to reveal out-of-plane susceptibility tensor components. A longpass dichroic mirror was used to separate the generated SHG from the fundamental and direct it onto a single channel detector (silicon avalanche photodiode, APD440A, Thorlabs). Co-polarized excitation–detection configuration and polarization rotation were achieved by positioning a linear polarizer and a half-waveplate between the objective and the dichroic mirror. Detection noise, substrate influence, and acceptance angle range were taken into account.

For wavelength-dependent SHG measurements in Figure 3, and SHG and THG measurements in Figure 1, a low-NA achromatic objective (NA = 0.3, 15x Reflective microscope objective, Thorlabs) was used with a co-polarized excitation and detection polarizers. For cryogenic measurements a He-flow cryostat (Cryovac) was used. The collected light was analyzed in a spectrometer coupled to a charged-coupled device (Horiba).

Supporting Information

Supporting Information is available from the Wiley Online Library or from the author.

Acknowledgements

S.T. acknowledges primary support from DOE-SC0020653 (materials synthesis), Applied Materials Inc., NSF CMMI 1825594 (NMR and TEM studies), NSF DMR-1955889 (magnetic measurements), NSF CMMI-1933214, NSF 1904716, NSF 1935994, NSF ECCS 2052527, DMR 2111812, and CMMI 2129412. K.M. and J.J.F. acknowledge support from the European Union Horizon 2020 research and innovation programme under Grant Agreement no. 820423 (S2QUIP) and the Deutsche Forschungsgemeinschaft (DFG, German Research Foundation) under Germany's Excellence Strategy – MCQST (EXC-2111), e-Conversion (EXC-2089), and via SPP 2299. M.M.P. acknowledges TUM International Graduate School of Science and Engineering (IGSSE). A.B.M. acknowledges funding from the International Max Planck Research School for Quantum Science and Technology (IMPRS-QST). M.B. and V.V. acknowledge the Alexander v. Humboldt foundation for financial support in the framework of their fellowship programs. K.M. acknowledges support from the Bayerische Akademie der Wissenschaften. G.S. acknowledges the German Research Foundation DFG (CRC 1375 NOA projects B5) and the IRTG 2675 META-ACTIVE (project A4).

Open access funding enabled and organized by Projekt DEAL.

Conflict of Interest

The authors declare no conflict of interest.

Author Contributions

M.M.P., G.S., J.J.F., and M.B. conceived and designed the experiment. Y.Q., Y.Sa., Y.Sh., and S.T. grew the Janus TMD monolayers, and A.B.M. fabricated the MoS_2 sample. M.M.P., V.V., P.H., and A.B.M. performed the optical measurements. M.M.P. analyzed the data and discussed them with all authors. M.M.P., G.S., and M.B. wrote the manuscript with input from all authors.

Data Availability Statement

The data that support the findings of this study are available from the corresponding author upon reasonable request.

Keywords

Janus TMD monolayers, MoSSe, nonlinear dispersion, out-of-plane SHG, WSSe

Received: April 24, 2023
Revised: June 29, 2023
Published online: August 1, 2023

[1] O. Dogadov, C. Trovatello, B. Yao, G. Soavi, G. Cerullo, *Laser Photonics Rev.* **2022**, *16*, 2100726.

[2] S. Shree, D. Lagarde, L. Lombez, C. Robert, A. Balocchi, K. Watanabe, T. Taniguchi, X. Marie, I. C. Gerber, M. M. Glazov, L. E. Golub, B. Urbaszek, I. Paradisanos, *Nat. Commun.* **2021**, *12*, 6894.
[3] I. Paradisanos, A. M. S. Raven, T. Amand, C. Robert, P. Renucci, K. Watanabe, T. Taniguchi, I. C. Gerber, X. Marie, B. Urbaszek, *Phys. Rev. B* **2022**, *105*, 115420.
[4] K.-Q. Lin, S. Bange, J. M. Lupton, *Nat. Phys.* **2019**, *15*, 242.
[5] G. Soavi, G. Wang, H. Rostami, D. G. Purdie, D. De Fazio, T. Ma, B. Luo, J. Wang, A. K. Ott, D. Yoon, S. A. Bourelle, J. E. Muench, I. Goykhman, S. Dal Conte, M. Celebrano, A. Tomadin, M. Polini, G. Cerullo, A. C. Ferrari, *Nat. Nanotechnol.* **2018**, *13*, 583.
[6] S. Klimmer, O. Ghaebi, Z. Gan, A. George, A. Turchanin, G. Cerullo, G. Soavi, *Nat. Photonics* **2021**, *15*, 837.
[7] Y. Zhang, Y. Wang, Y. Dai, X. Bai, X. Hu, L. Du, H. Hu, X. Yang, D. Li, Q. Dai, T. Hasan, Z. Sun, *Sci. Adv.* **2022**, *8*, eabq8246.
[8] Y. Li, N. An, Z. Lu, Y. Wang, B. Chang, T. Tan, X. Guo, X. Xu, J. He, H. Xia, Z. Wu, Y. Su, Y. Liu, Y. Rao, G. Soavi, B. Yao, *Nat. Commun.* **2022**, *13*, 3138.
[9] N. An, T. Tan, Z. Peng, C. Qin, Z. Yuan, L. Bi, C. Liao, Y. Wang, Y. Rao, G. Soavi, B. Yao, *Nano Lett.* **2020**, *20*, 6473.
[10] A. Dasgupta, J. Gao, X. Yang, *Nano Lett.* **2019**, *19*, 6511.
[11] Q. Guo, X.-Z. Qi, L. Zhang, M. Gao, S. Hu, W. Zhou, W. Zang, X. Zhao, J. Wang, B. Yan, M. Xu, Y.-K. Wu, G. Eda, Z. Xiao, S. A. Yang, H. Gou, Y. P. Feng, G.-C. Guo, W. Zhou, X.-F. Ren, C.-W. Qiu, S. J. Pennycook, A. T. S. Wee, *Nature* **2023**, *613*, 53.
[12] F. Li, W. Wei, P. Zhao, B. Huang, Y. Dai, *J. Phys. Chem. Lett.* **2017**, *8*, 5959.
[13] J. Wang, H. Shu, T. Zhao, P. Liang, N. Wang, D. Cao, X. Chen, *Phys. Chem. Chem. Phys.* **2018**, *20*, 18571.
[14] W. Shi, Z. Wang, *J. Phys.: Condens. Matter* **2018**, *30*, 215301.
[15] Y. C. Cheng, Z. Y. Zhu, M. Tahir, U. Schwingenschlögl, *EPL (Europhys. Lett.)* **2013**, *102*, 57001.
[16] C. Cheng, J.-T. Sun, X.-R. Chen, H.-X. Fu, S. Meng, *Nanoscale* **2016**, *8*, 17854.
[17] Q.-F. Yao, J. Cai, W.-Y. Tong, S.-J. Gong, J.-Q. Wang, X. Wan, C.-G. Duan, J. H. Chu, *Phys. Rev. B* **2017**, *95*, 165401.
[18] T. Hu, F. Jia, G. Zhao, J. Wu, A. Stroppa, W. Ren, *Phys. Rev. B* **2018**, *97*, 235404.
[19] Moh. Adhib Ulil Absor, H. Kotaka, F. Ishii, M. Saito, *Jpn. J. Appl. Phys.* **2018**, *57*, 04FP01.
[20] S. Patel, U. Dey, N. P. Adhikari, A. Taraphder, *Phys. Rev. B* **2022**, *106*, 035125.
[21] J. Yuan, Y. Yang, Y. Cai, Y. Wu, Y. Chen, X. Yan, L. Shen, *Phys. Rev. B* **2020**, *101*, 094420.
[22] J. Liang, W. Wang, H. Du, A. Hallal, K. Garcia, M. Chshiev, A. Fert, H. Yang, *Phys. Rev. B* **2020**, *101*, 184401.
[23] Q. Cui, J. Liang, Z. Shao, P. Cui, H. Yang, *Phys. Rev. B* **2020**, *102*, 094425.
[24] H. Jin, T. Wang, Z.-R. Gong, C. Long, Y. Dai, *Nanoscale* **2018**, *10*, 19310.
[25] F. Li, W. Wei, H. Wang, B. Huang, Y. Dai, T. Jacob, *J. Phys. Chem. Lett.* **2019**, *10*, 559.
[26] C. Long, Y. Dai, Z.-R. Gong, H. Jin, *Phys. Rev. B* **2019**, *99*, 115316.
[27] T. Zheng, Y.-C. Lin, Y. Yu, P. Valencia-Acuna, A. A. Puretzky, R. Torsi, C. Liu, I. N. Ivanov, G. Duscher, D. B. Geohegan, Z. Ni, K. Xiao, H. Zhao, *Nano Lett.* **2021**, *21*, 931.
[28] H. Guo, X. Zhang, G. Lu, *Sci. Adv.* **2022**, *8*, eabp9757.
[29] A.-Y. Lu, H. Zhu, J. Xiao, C.-P. Chuu, Y. Han, M.-H. Chiu, C.-C. Cheng, C.-W. Yang, K.-H. Wei, Y. Yang, Y. Wang, D. Sokaras, D. Nordlund, P. Yang, D. A. Muller, M.-Y. Chou, X. Zhang, L.-J. Li, *Nat. Nanotechnol.* **2017**, *12*, 744.
[30] J. Zhang, S. Jia, I. Kholmanov, L. Dong, D. Er, W. Chen, H. Guo, Z. Jin, V. B. Shenoy, L. Shi, J. Lou, *ACS Nano* **2017**, *11*, 8192.
[31] D. Lam, D. Lebedev, M. C. Hersam, *ACS Nano* **2022**, *16*, 7144.
[32] Y.-C. Lin, C. Liu, Y. Yu, E. Zarkadoula, M. Yoon, A. A. Puretzky, L. Liang, X. Kong, Y. Gu, A. Strasser, H. M. Meyer, M. Lorenz, M. F. Chisholm, I. N. Ivanov, C. M. Rouleau, G. Duscher, K. Xiao, D. B. Geohegan, *ACS Nano* **2020**, *14*, 3896.
[33] D. B. Trivedi, G. Turgut, Y. Qin, M. Y. Sayyad, D. Hajra, M. Howell, L. Liu, S. Yang, N. H. Patoary, H. Li, M. M. Petrić, M. Meyer, M. Kremser, M. Barbone, G. Soavi, A. V. Stier, K. Müller, S. Yang, I. S. Esqueda, H. Zhuang, J. J. Finley, S. Tongay, *Adv. Mater.* **2020**, *32*, 2006320.
[34] Y. Guo, Y. Lin, K. Xie, B. Yuan, J. Zhu, P.-C. Shen, A.-Y. Lu, C. Su, E. Shi, K. Zhang, C. HuangFu, H. Xu, Z. Cai, J.-H. Park, Q. Ji, J. Wang, X. Dai, X. Tian, S. Huang, L. Dou, L. Jiao, J. Li, Y. Yu, J.-C. Idrobo, T. Cao, T. Palacios, J. Kong, *Proc. Natl. Acad. Sci. USA* **2021**, *118*, e2106124118.
[35] C. W. Jang, W. J. Lee, J. K. Kim, S. M. Park, S. Kim, S.-H. Choi, *NPG Asia Mater.* **2022**, *14*, 15.
[36] Y. Qin, M. Sayyad, A. R.-P. Montblanch, M. S. G. Feuer, D. Dey, M. Blei, R. Sailus, D. M. Kara, Y. Shen, S. Yang, A. S. Botana, M. Atature, S. Tongay, *Adv. Mater.* **2022**, *34*, 2106222.
[37] Z. Gan, I. Paradisanos, A. Estrada-Real, J. Picker, E. Najafidehaghani, F. Davies, C. Neumann, C. Robert, P. Wiecha, K. Watanabe, T. Taniguchi, X. Marie, J. Biskupek, M. Mundszinger, R. Leiter, U. Kaiser, A. V. Krasheninnikov, B. Urbaszek, A. George, A. Turchanin, *Adv. Mater.* **2022**, *34*, 2205226.
[38] S. B. Harris, Y.-C. Lin, A. A. Puretzky, L. Liang, O. Dyck, T. Berlijn, G. Eres, C. M. Rouleau, K. Xiao, D. B. Geohegan, *ACS Nano* **2023**, *17*, 2472.
[39] M. M. Petrić, M. Kremser, M. Barbone, Y. Qin, Y. Sayyad, Y. Shen, S. Tongay, J. J. Finley, A. R. Botello-Méndez, K. Müller, *Phys. Rev. B* **2021**, *103*, 035414.
[40] K. Zhang, Y. Guo, D. T. Larson, Z. Zhu, S. Fang, E. Kaxiras, J. Kong, S. Huang, *ACS Nano* **2021**, *15*, 14394.
[41] K. Zhang, Y. Guo, Q. Ji, A.-Y. Lu, C. Su, H. Wang, A. A. Puretzky, D. B. Geohegan, X. Qian, S. Fang, E. Kaxiras, J. Kong, S. Huang, *J. Am. Chem. Soc.* **2020**, *142*, 17499.
[42] T. Zheng, Y.-C. Lin, N. Rafizadeh, D. B. Geohegan, Z. Ni, K. Xiao, H. Zhao, *ACS Nano* **2022**, *16*, 4197.
[43] M. S. G. Feuer, A. R.-P. Montblanch, M. Y. Sayyad, C. M. Purser, Y. Qin, E. M. Alexeev, A. R. Cadore, B. L. T. Rosa, J. Kerfoot, E. Mostaani, R. Kalęba, P. Kolari, J. Kopaczek, K. Watanabe, T. Taniguchi, A. C. Ferrari, D. M. Kara, S. Tongay, M. Atatüre, *ACS Nano* **2023**, *17*, 7326.
[44] C. Bian, J. Shi, X. Liu, Y. Yang, H. Yang, H. Gao, *Chin. Phys. B* **2022**, *31*, 097304.
[45] J. Zhang, X. Wen, T. Zhai, G. P. Wiederrecht, J. Lou, *2D Mater.* **2022**, *9*, 035006.
[46] N. Youngblood, M. Li, *Nanophotonics* **2016**, *6*, 1205.
[47] P. Tonndorf, O. Del Pozo-Zamudio, N. Gruhler, J. Kern, R. Schmidt, A. I. Dmitriev, A. P. Bakhtinov, A. I. Tartakovskii, W. Pernice, S. Michaelis de Vasconcellos, R. Bratschitsch, *Nano Lett.* **2017**, *17*, 5446.
[48] Y. Guo, Z. Li, N. An, Y. Guo, Y. Wang, Y. Yuan, H. Zhang, T. Tan, C. Wu, B. Peng, G. Soavi, Y. Rao, B. Yao, *Adv. Mater.* **2022**, *34*, 2207777.
[49] G. Q. Ngo, E. Najafidehaghani, Z. Gan, S. Khazaee, M. P. Siems, A. George, E. P. Schartner, S. Nolte, H. Ebendorff-Heidepriem, T. Pertsch, A. Tuniz, M. A. Schmidt, U. Peschel, A. Turchanin, F. Eilenberger, *Nat. Photonics* **2022**, *16*, 769.
[50] A. Autere, H. Jussila, A. Marini, J. R. M. Saavedra, Y. Dai, A. Säynätjoki, L. Karvonen, H. Yang, B. Amirsolaimani, R. A. Norwood, N. Peyghambarian, H. Lipsanen, K. Kieu, F. J. G. de Abajo, Z. Sun, *Phys. Rev. B* **2018**, *98*, 115426.
[51] M. Zhao, Z. Ye, R. Suzuki, Y. Ye, H. Zhu, J. Xiao, Y. Wang, Y. Iwasa, X. Zhang, *Light: Sci. Appl.* **2016**, *5*, e16131.
[52] C. Trovatello, A. Marini, X. Xu, C. Lee, F. Liu, N. Curreli, C. Manzoni, S. Dal Conte, K. Yao, A. Ciattoni, J. Hone, X. Zhu, P. J. Schuck, G. Cerullo, *Nat. Photonics* **2021**, *15*, 6.
[53] Y. Wei, X. Xu, S. Wang, W. Li, Y. Jiang, *Phys. Chem. Chem. Phys.* **2019**, *21*, 21022.

[54] A. Strasser, H. Wang, X. Qian, *Nano Lett.* **2022**, *22*, 4145.
[55] N. A. Pike, R. Pachter, *J. Phys. Chem. C* **2022**, *126*, 16243.
[56] M.-E. Kleemann, R. Chikkaraddy, E. M. Alexeev, D. Kos, C. Carnegie, W. Deacon, A. C. de Pury, C. Große, B. de Nijs, J. Mertens, A. I. Tartakovskii, J. J. Baumberg, *Nat. Commun.* **2017**, *8*, 1296.
[57] M. Stührenberg, B. Munkhbat, D. G. Baranov, J. Cuadra, A. B. Yankovich, T. J. Antosiewicz, E. Olsson, T. Shegai, *Nano Lett.* **2018**, *18*, 5938.
[58] J. Zhang, W. Zhao, P. Yu, G. Yang, Z. Liu, *2D Mater.* **2020**, *7*, 042002.
[59] Y. R. Shen, *The Principles of Nonlinear Optics*, Wiley Classics Library ed., Wiley-Interscience, Hoboken, N.J **2003**.
[60] R. W. Boyd, *Nonlinear Optics*, 3rd ed., Academic Press, Amsterdam; Boston **2008**.
[61] P. A. Franken, A. E. Hill, C. W. Peters, G. Weinreich, *Phys. Rev. Lett.* **1961**, *7*, 118.
[62] I. Paradisanos, G. Wang, E. M. Alexeev, A. R. Cadore, X. Marie, A. C. Ferrari, M. M. Glazov, B. Urbaszek, *Nat. Commun.* **2021**, *12*, 538.
[63] G. Wang, X. Marie, I. Gerber, T. Amand, D. Lagarde, L. Bouet, M. Vidal, A. Balocchi, B. Urbaszek, *Phys. Rev. Lett.* **2015**, *114*, 097403.
[64] L. M. Malard, T. V. Alencar, A. P. M. Barboza, K. F. Mak, A. M. de Paula, *Phys. Rev. B* **2013**, *87*, 201401.
[65] N. Kumar, S. Najmaei, Q. Cui, F. Ceballos, P. M. Ajayan, J. Lou, H. Zhao, *Phys. Rev. B* **2013**, *87*, 161403.
[66] R. Wang, H.-C. Chien, J. Kumar, N. Kumar, H.-Y. Chiu, H. Zhao, *ACS Appl. Mater. Interfaces* **2014**, *6*, 314.
[67] R. I. Woodward, R. T. Murray, C. F. Phelan, R. E. P. de Oliveira, T. H. Runcorn, E. J. R. Kelleher, S. Li, E. C. de Oliveira, G. J. M. Fechine, G. Eda, C. J. S. de Matos, *2D Mater.* **2016**, *4*, 011006.
[68] A. Säynätjoki, L. Karvonen, H. Rostami, A. Autere, S. Mehravar, A. Lombardo, R. A. Norwood, T. Hasan, N. Peyghambarian, H. Lipsanen, K. Kieu, A. C. Ferrari, M. Polini, Z. Sun, *Nat. Commun.* **2017**, *8*, 893.
[69] H. G. Rosa, Y. W. Ho, I. Verzhbitskiy, M. J. F. L. Rodrigues, T. Taniguchi, K. Watanabe, G. Eda, V. M. Pereira, J. C. V. Gomes, *Sci. Rep.* **2018**, *8*, 10035.
[70] A. Kormányos, V. Zólyomi, N. D. Drummond, P. Rakyta, G. Burkard, V. I. Fal'ko, *Phys. Rev. B* **2013**, *88*, 045416.
[71] Y. Li, Y. Rao, K. F. Mak, Y. You, S. Wang, C. R. Dean, T. F. Heinz, *Nano Lett.* **2013**, *13*, 3329.
[72] J. Xiao, H. Zhu, Y. Wang, W. Feng, Y. Hu, A. Dasgupta, Y. Han, Y. Wang, D. A. Muller, L. W. Martin, P. Hu, X. Zhang, *Phys. Rev. Lett.* **2018**, *120*, 227601.
[73] L. Lafeta, A. Corradi, T. Zhang, E. Kahn, I. Bilgin, B. R. Carvalho, S. Kar, M. Terrones, L. M. Malard, *2D Mater.* **2021**, *8*, 035010.